ACS Catalysis

pubs.acs.org/acscatalysis Research Article

Role of Surface Hydrogen Coverage in C−C Coupling Process for CO_2 Electroreduction on Ni-Based Catalysts

Haowen Ding, Shisheng Zheng,* Xinzhe Yang, Junjie Pan, Zhefeng Chen, Mingzheng Zhang, Shunning Li,* and Feng Pan*

Cite This: *ACS Catal.* 2024, 14, 14330−14338 Read Online

ACCESS | Metrics & More | Article Recommendations | Supporting Information

ABSTRACT: Research into electrochemical CO_2 reduction reaction (CO_2RR) toward multicarbon products has long been dominated by the investigation of Cu-based catalyst system. Yet, several recent studies have documented competitive catalytic performance on Ni-based alloys and compounds, which can trigger C−C coupling for producing long-chain hydrocarbons. To develop an in-depth understanding of how Ni-based catalysts carry out C−C coupling, here we present a comparative study of Ni metal and Ni_3Ga via density functional theory calculations. Inspiringly, unlike Ni metal where the distribution of hydrogen adsorbates on the surface is found irregular during CO_2RR, Ni_3Ga exhibits a perfectly ordered distribution pattern of surface hydrogen at a low coverage when CO_2 is reduced into intermediates ready for C−C coupling. This difference in adsorbate coverage leads to scenarios in which neighboring CO_2RR intermediates on Ni metal tend to be separated by a large distance, whereas they can be accommodated much closer on Ni_3Ga surface, thus creating the opportunity for the coupling reaction. This mechanistic insight finds support from previous experimental reports, and can establish surface hydrogen coverage as a nonnegligible factor for C−C coupling on Ni-based catalysts.

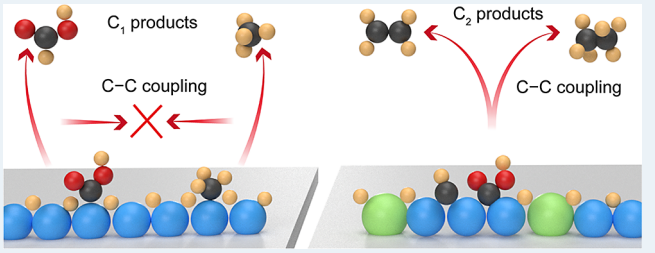

KEYWORDS: *surface hydrogen coverage, carbon dioxide reduction, multicarbon products, nickel-based electrocatalysts, density functional theory*

INTRODUCTION

Renewable electricity-driven reduction of CO_2 to multicarbon (C_{2+}) products has been identified as a promising avenue to alleviating the greenhouse effect and meanwhile producing the value-added hydrocarbon chemicals that are currently supplied from fossil fuels.[1−3] Although many heterogeneous catalysts have been developed for this purpose, they are almost universally restricted to specific C_2 products such as ethylene and ethanol.[4−6] Selective formation of longer-chain carbon products is generally beyond attainment. The challenge, as suggested by a plethora of experimental and theoretical studies,[7−9] lies in the C−C coupling process, which is decisive in the pathways to C_{2+} products in CO_2 reduction reaction (CO_2RR) but suffers from sluggish kinetics at ambient conditions.[10,11] Recently, Ni-based alloys and compounds have emerged as an intriguing electrocatalyst system that exhibits unprecedentedly high selectivity toward C_3 and C_4 hydrocarbons.[12−14] Unlike the Cu metal catalyst that is well-known for its ability to produce considerable amounts of ethylene in CO_2RR even without the incorporation of any other elements,[15−17] the Ni metal exhibits inferior catalytic efficiency unless mixing with a proper element, such as O, P or Ga.[18−22] This indicates a critical interplay between Ni and other atoms to steer the reaction pathways to C_{2+} products. However, the limited studies on Ni-based catalysts so far fail to bring the mechanisms of this interplay to the same level of understanding as that on Cu-based counterparts.[23−26] Especially, it remains elusive how the C−C coupling process is controlled by the constituent elements in these Ni-based catalysts, not to mention that the subtle influence of their surface geometric structures is poorly understood.[27−29]

In the recent work by Zhou et al.,[20] it was proposed that the facile C−C coupling on Ni-based catalysts is closely associated with the polarization of the Ni sites, which arises from the interaction with elements showing a high degree of electronegativity, such as O. However, such a mechanism cannot easily explain the C_{2+} selectivity on some catalysts that exhibit much less pronounced polarization, such as Ni−P and Ni−Ga compounds.[12,13,18,19] Our previous investigation on Ni_2P supported a mechanistic scenario that the trinuclear Ni_3 sites at the surface could cooperatively accommodate the reaction

Received: April 10, 2024
Revised: June 28, 2024
Accepted: September 4, 2024
Published: September 12, 2024

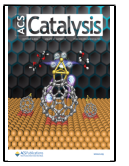

https://doi.org/10.1021/acscatal.4c02126
ACS Catal. 2024, 14, 14330−14338

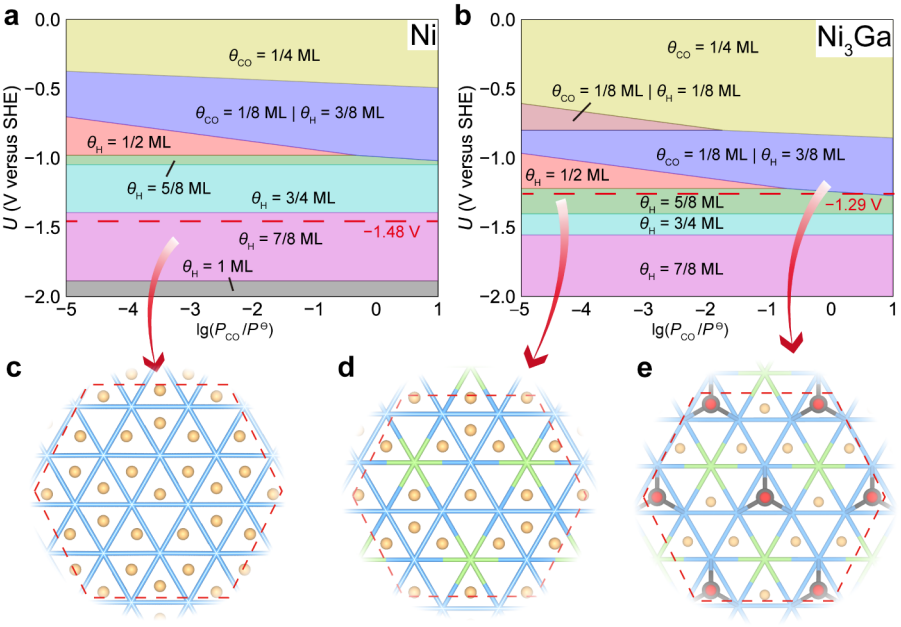

Figure 1. Thermodynamics of surface adsorbates and the corresponding distribution patterns. (a, b) Pourbaix diagrams of (a) Ni (111) and (b) Ni_3Ga (111) surfaces. (c) Distribution patterns of *H on Ni (111) at pH = 6.8 and $U = -1.48$ V versus SHE. (d, e) Distribution patterns of *CO/*H on Ni_3Ga (111) at pH = 6.8 and $U = -1.29$ V versus SHE with (d) low $CO_{(g)}$ pressure and (e) high $CO_{(g)}$ pressure. Top view is provided for each distribution pattern, with a red dashed frame highlighting the region that we focused on when studying CO_2RR. The blue/green nodes of the triangular mesh denote the Ni/Ga atoms at the surface layer, while edges of the mesh denote their bonding. Color code for adsorbates: H, yellow; C, black; O, red.

intermediates in CO_2RR and promote interfacial proton transfer to overcome the kinetic limitation for C−C coupling.[30] Yet this scenario is not universal in the Ni-based catalysts, since the formation of surface trinuclear Ni_3 sites is by no means a common occurrence in other compounds.[31] Therefore, we believe that there are additional factors beyond these chemical and geometrical aspects in promoting C−C coupling. Thanks to recent studies reporting the effects conferred by the constituents of electrolytes,[32−34] we were inspired by the idea that the proton supply in the electric double layer, as modified by the electrolyte composition,[35−37] could play a pivotal role in C−C coupling process. Given the fact that the interfacial proton supply will also determine the coverage of *H atoms over the catalyst surface, which has already been demonstrated on Ni metal and Ni−P compounds,[38,39] it is likely that the hydrogen coverage could play a nontrivial role in the selectivity of electrochemical reactions. This hypothesis has been largely unexplored in previous studies on CO_2RR, but it is compatible with the literature where hydrogen adsorbate coverage was shown critical for the facile electrocatalytic reduction of N_2.[40]

Here to test this hypothesis, we employ Ni_3Ga catalyst as an example, which has previously demonstrated an ability to realize the electrochemical reduction of CO_2 to C_{2+} products. We note that the electronegativity of Ga is relatively close to Ni, and that the Ni_3Ga (111) surface is not only stable but isostructural to Ni (111).[41] These features make it possible to minimize the contribution from atom polarization and geometrical factors when comparing the catalytic performance between Ni_3Ga and Ni metal. While hydrogen adsorption is likely to occur at a very negative potential, we should not ignore the impact of CO poisoning on Ni-based catalysts, which was demonstrated to be profound before the potential is low enough for hydrogen evolution reaction (HER) to take the lead in all the reduction reactions.[42,43] Moreover, since the reaction path of CO_2RR on Ni-based catalysts was proposed to be different from that on Cu[20,44] we should not simply adopt the theory proposed in Cu catalyst for the investigation of Ni and Ni_3Ga.

In this work, using systematic density functional theory (DFT) calculations, we have compared the adsorbate configurations between Ni and Ni_3Ga in CO_2RR, with *H and *CO taken as the possible adsorbates. We discover that under optimal working conditions, both Ni and Ni_3Ga surfaces are dominated by *H species, while they display a large difference in the distribution pattern of *H. During CO_2RR, some of the *H adsorbates can be consumed by the reaction intermediates, and the remaining *H atoms on Ni_3Ga surface will exhibit a highly symmetric and ordered configuration at an adsorbate coverage of 1/2 monolayer (ML). In contrast, the hydrogen coverage on Ni surface is considerably higher, and the distribution of *H is more irregular than on Ni_3Ga throughout the CO_2-to-C_1 (C_1: single-carbon species) reaction. We further discover that the ordering of adsorbates on Ni_3Ga at 1/2 ML coverage could lead to an allocation of two C_1 reaction intermediates at close vicinity, which is vital to boost the C−C coupling efficiency. This mechanism of low-coverage-induced hydrogen ordering can offer a causal explanation for the promising C_{2+} selectivity exhibited on a series of Ni-based alloys/compounds, and can be further exploited as a strategy to screen for potential CO_2RR catalysts beyond Ni- or Cu-based materials.

RESULTS AND DISCUSSION

Surface Hydrogen Coverage. We first investigate the possibility of adsorption for *H, *OH and *CO species. Configurations of individual adsorbates are considered, and their adsorption energies on Ni (111) and Ni_3Ga (111)

https://doi.org/10.1021/acscatal.4c02126
ACS Catal. 2024, 14, 14330−14338

surfaces are provided in Figure S1. *CO adsorbate exhibits a much more negative adsorption energy than the other two species, and the adsorption energy of *OH species is close to 0 eV at both Ni and Ni_3Ga surfaces. We note that the adsorption energy of *OH will become more positive at a more negative potential according to $H_2O + * + h^+ \rightleftharpoons *OH + H^+$. If we consider the reaction of $H_2O + * \rightleftharpoons *OH + *H$, the free energy change (−0.58 and −0.67 eV for Ni and Ni_3Ga, respectively) is independent of the applied potential and pH. Yet, this value is much higher than that of CO adsorption (free energy changes at a low CO pressure of 10^{-5} bar are −1.08 and −1.32 eV for Ni and Ni_3Ga, respectively). Therefore, the *OH + *H coadsorption configuration is energetically unfavorable when in competition with *CO adsorption. Overall, from a thermodynamic perspective, *OH adsorption at the catalyst surface is unlikely to take place under the working conditions, and is thus left out of the following calculations.

According to the calculated surface energies with different adsorbate configurations, the Pourbaix diagrams can be constructed for both Ni and Ni_3Ga surfaces. All the configurations taken into account in the Pourbaix diagram calculations are tabulated in Table S1. To resolve the discrepancy between DFT and experimental results regarding the gas-phase reference energies of CO_2 and CO molecules, we have applied energy corrections of +0.24 eV and −0.19 eV, respectively, according to the study of Granda-Marulanda et al.[45] For each level of adsorbate coverage, the Ewald summation method[46] was employed to determine the most probable configuration of hydrogen distribution, and its structure was further relaxed using DFT calculations. It is worth mentioning that in previous experimental studies,[43,47] the optimal working condition for electrochemical CO_2RR on Ni metal was pH = 6.8 and U = −1.48 V versus standard hydrogen electrode (SHE), while the best performance on Ni_3Ga was achieved at pH = 6.8 and U = −1.29 V versus SHE. Here, the Pourbaix diagrams are constructed as a function of P_{CO} and U, with pH = 6.8. P_{CO} is used as one of the attributes because the potential independent step of CO desorption is the determinant for CO coverage at the surface. As shown in Figure 1a,b, both Ni and Ni_3Ga surfaces are covered by *CO adsorbates at $U > -0.5$ V, in agreement with experimental findings of CO poisoning.[48] As the potential decreases, *CO is replaced by *H, which is reminiscent of the previous calculation results on Cu surface.[49] Under working conditions (indicated by the red dashed line in Figure 1a,b), the main surface adsorbates are *H on both catalysts. The configuration on Ni surface is θ_H = 7/8 ML, while there are two situations on Ni_3Ga: at low P_{CO}, the adsorbate configuration is θ_H = 5/8 ML, and at high P_{CO}, it is θ_{CO} = 1/8 ML | θ_H = 3/8 ML.

The hydrogen distribution patterns on Ni and Ni_3Ga are depicted in Figure 1c−e, showing that the differences not only manifest in the number of surface adsorbates, but also in their location. On Ni (111) surface, some of the *H adsorbates are lying in between the hollow and bridge sites (Figure S2), while on Ni_3Ga (111) all the adsorbates are accommodated exactly at the hollow sites. Given that the hollow sites are more energetically favorable than other sites for an isolated *H on Ni, the configuration shown in Figure 1c would imply that the overall electronic repulsion between neighboring *H species has slightly surpassed the interaction between *H and the surface Ni atoms. This confers a relatively strong propensity for *H to interact with the reaction intermediates of CO_2RR, which will be discussed in the following sections. According to the Bader charge analysis, Ga atoms on Ni_3Ga (111) surface exist in a valence state of +0.31 and Ni atoms are negatively charged (Figure S3). It suggests that the atom polarization is much weaker for Ni_3Ga when compared to the Ni−O system investigated in previous studies.[20,50] Apart from the polarization effect, the weaker binding of *H to Ga than to Ni (Table S2) is a key characteristic that dictates the distribution pattern of adsorbates. On one hand, the weak Ga−H affinity leads to lower hydrogen coverage on Ni_3Ga (111) than on Ni (111) at the same P_{CO} and U values. On the other hand, this characteristic could account for the observation that in a low-P_{CO} environment, the Ni_3-hollow sites (Ni_3 here means the location above three neighboring Ni atoms) are fully occupied on the Ni_3Ga (111) surface at 5/8 ML hydrogen coverage, with the rest of *H distributed at the Ni_2Ga-hollow sites. Notably, this distribution pattern is commensurate to the 3-fold symmetric structure of the Ni_3Ga (111) surface, and similar structure of symmetric ordering can also be observed at 5/8 ML hydrogen coverage on Ni (111) (Figure S4). Such an ordering of surface hydrogen is reminiscent of that reported on other metal surfaces, such as Pd (111),[51,52] where *H species coalesce into a 3-fold symmetric structure with a local coverage of 2/3 ML. In a high-P_{CO} environment, *CO adsorbates will replace some of the *H atoms at Ni_3-hollow sites, and only the *H atoms at Ni_2Ga-hollow sites can remain on the surface. This corresponds to an ordered pattern with an adsorbate coverage of 1/2 ML by adding up both *CO and *H species. All the above results indicate that the Ga atoms in Ni_3Ga can function as a modulator to dilute *H adsorbates to a level where their mutual electronic interaction is no longer strong enough to disturb their symmetric distribution.

Evolution of Hydrogen Distribution Patterns during Reactions. We first examine the reaction path from CO_2 to $*C_1$ intermediates on Ni (111) surface at pH = 6.8 and U = −1.48 V versus SHE. This condition provides an initial hydrogen coverage of 7/8 ML. The free energy profile is displayed in Figure 2, along with the evolution of adsorbate coverage in the vicinity of the reaction center. We note that two possible mechanisms have been evaluated in the DFT calculation for each elementary step. One is the proton-coupled electron transfer (PCET) process, and the other is proton translocation (PT) from catalyst surface to the reaction intermediate. The former process is potential dependent, where protons are transported from the electrolyte to the intermediate, accompanied by one-electron transfer to the catalytic center. In contrast, the latter process is potential independent, with a *H adsorbate directly consumed at the surface for the hydrogenation of a CO_2RR intermediate. Our results show that the first hydrogenation step of CO_2 on Ni proceeds via the latter process, which is 0.24 eV lower in free energy change than the former one. Given that each of the $*C_1$ intermediates can only occupy one adsorption site at the surface (among top site, bridge site and hollow site), $*C_1$ species and *H are here treated identical when calculating the adsorbate coverage. Therefore, the adsorbate coverage remains unchanged at the first hydrogenation step of CO_2, in which a *H adsorbate is assumed to be replaced by *COOH. Subsequent hydrogenation steps toward $*CH_3$ will consume two additional *H, leading to an adsorbate coverage of 13/16 ML eventually. The possible routes to other reaction intermediates are demonstrated in Figure S5, and the corresponding structures are displayed in Figure S6.

https://doi.org/10.1021/acscatal.4c02126
ACS Catal. 2024, 14, 14330−14338

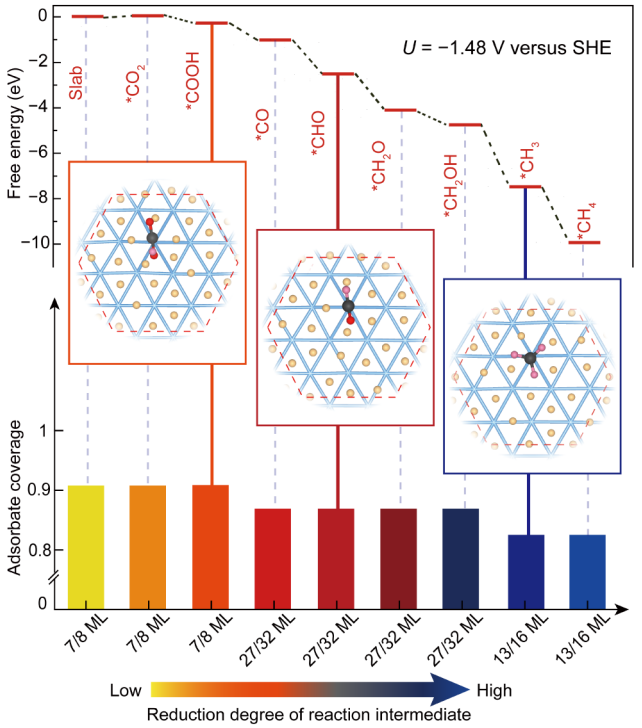

Figure 2. Free energy diagram for the reaction path from CO_2 to $*C_1$ intermediates on Ni (111) at pH = 6.8 and $U = -1.48$ V versus SHE. The insets show three of the critical reaction intermediates. The evolution of adsorbate coverage is also demonstrated, along with the reduction degree of the intermediates. An elementary step with a changed coverage corresponds to PT mechanism, while a step with unchanged coverage corresponds PCET mechanism. $*CH_2$ is not presented in the diagram because this adsorbate is unstable upon structural optimization and will spontaneously transform into $*CH_3$ by capturing a *H atom from the surface. Color code: Ni, blue; C, black; O, red; *H adsorbate, yellow; H atom in a CO_2 reduction intermediate, pink.

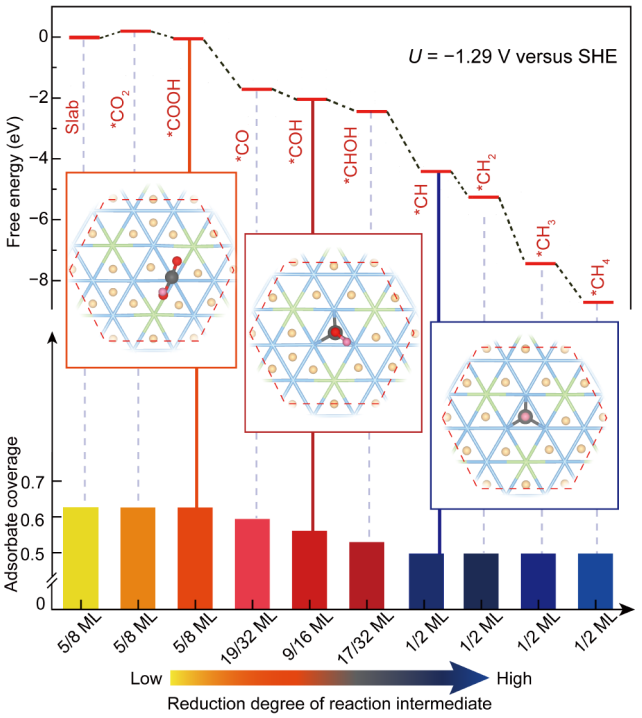

Figure 3. Free energy diagram for the reaction path from CO_2 to $*C_1$ intermediates on Ni_3Ga (111) at pH = 6.8, $U = -1.29$ V versus SHE and low P_{CO}. The insets show three of the critical reaction intermediates. The evolution of adsorbate coverage is also demonstrated, along with the reduction degree of the intermediates. An elementary step with a changed coverage corresponds to PT mechanism, while a step with unchanged coverage corresponds PCET mechanism. Color code: Ni, blue; Ga, green; C, black; O, red; *H adsorbate, yellow; H atom in a CO_2 reduction intermediate, pink.

CO_2RR on Ni_3Ga (111) at pH = 6.8 and $U = -1.29$ V versus SHE adopts a different reaction path from the above results for Ni. Figure 3 shows the calculation results for Ni_3Ga in a low-P_{CO} environment. We note that on Ni (111), the hydrogenation of *CO results in *CHO, followed by $*CH_2O$, $*CH_2OH$ and $*CH_3$ (we note that $*CH_2$ is unstable and will spontaneously transform into $*CH_3$ by capturing a *H atom from the surface), while on Ni_3Ga (111), *CO will be sequentially reduced to *COH, *CHOH, *CH, $*CH_2$ and $*CH_3$. The difference in reaction path is probably linked with the higher hydrogen coverage on Ni than on Ni_3Ga. Specifically, *CHO tends to occupy the top site on Ni surface with some of its neighboring hollow sites occupied by *H, while *COH favors the hollow site, thus driving a competition between *COH and *H because the number of vacant hollow sites on the surface is limited at high hydrogen coverage. This competition may incur an energy penalty for *COH formation as compared to *CHO due to the strong repulsion between *H species on Ni (111). In contrast, the relatively lower hydrogen coverage on Ni_3Ga (111) leads to a picture in which there are so many vacant hollow sites for *H species that they can be distributed away from the reaction intermediates (Figure S7). Therefore, the electrostatic interaction between *CHO/*COH and surface hydrogen is less intense than that on Ni. Furthermore, the *CHO adsorbate is trapped near the hollow site on Ni_3Ga surface, probably due to the 3-fold symmetric distribution of Ga at the surface layer. This mismatches with the tendency of forming only one metal−carbon bond for *CHO as often seen in other metal catalysts,[25,53−55] which can potentially explain the higher stability of *COH than *CHO on Ni_3Ga (111) (Figure S8). We have further calculated the kinetic energy barriers for *CO → *CHO and *CO → *COH steps on Ni (111) and Ni_3Ga (111). On Ni, the barriers for the formation of *CHO and *COH are 0.21 and 0.51 eV, respectively (Figures S10 and S11), while the corresponding values on Ni_3Ga are 0.70 and 0.19 eV, respectively (Figures S12 and S13). Therefore, the hydrogenation of *CO adopts the CHO pathway on Ni and the COH pathway on Ni_3Ga, which is consistent with the thermodynamic calculations displayed above.

Figure 4 shows the free energy diagram for the reaction on Ni_3Ga in a high-P_{CO} environment, taking the adsorbate configuration shown in Figure 1e as the initial state. The possible routes to other reaction intermediates and the corresponding structures are displayed in Figures S14 and S15. Notably, the adsorbate coverage at high P_{CO} remains at 1/2 ML throughout *CO → $*CH_3$, suggesting that this adsorbate distribution pattern would always be at play in the C−C coupling process. If we assume *CO and *H to be identical, it is surprising to see that the adsorbate pattern in Figure 4 is exactly the same as the final pattern displayed in Figure 3 after the adsorbate coverage is reduced to 1/2 ML (corresponding to *CH, $*CH_2$, $*CH_3$ and $*CH_4$ reaction

https://doi.org/10.1021/acscatal.4c02126
ACS Catal. 2024, 14, 14330−14338

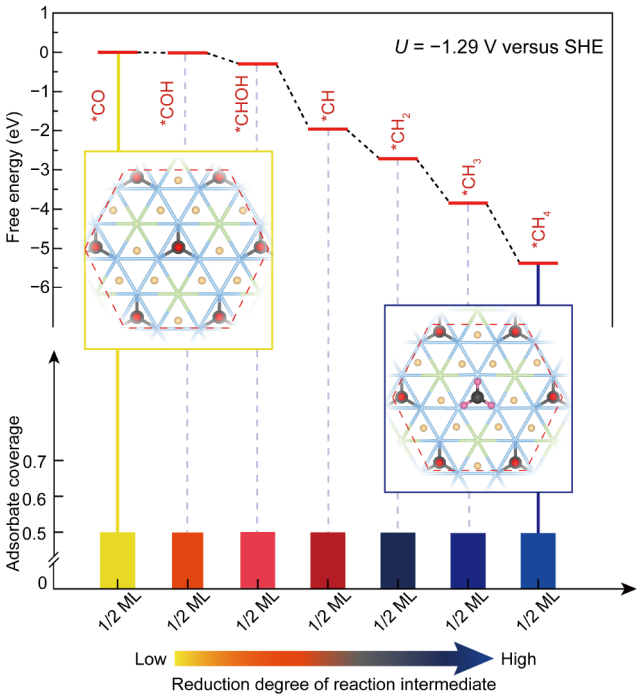

Figure 4. Free energy diagram for the reaction path from *CO to *C_1 intermediates on Ni_3Ga (111) at pH = 6.8, U = −1.29 V versus SHE and high P_{CO}. The insets show the initial and final reaction intermediates. The evolution of adsorbate coverage is also demonstrated, along with the reduction degree of the intermediates. All the elementary steps proceed via the PCET mechanism. Color code: Ni, blue; Ga, green; C, black; O, red; *H adsorbate, yellow; H atom in a CO_2 reduction intermediate, pink.

intermediates). It means that when the *CH_x (x = 1−3) intermediates participate in C−C coupling, the local environment at the catalytic center (surrounded by six *H adsorbates symmetrically) would be nearly the same for different P_{CO}. Given the recent experimental evidence suggesting *CH_x as the potential coupling intermediate for C_{2+} products,[20] our results could imply that the *CO coverage on Ni_3Ga at high P_{CO} would be too sparse to exert influence on C−C coupling under working conditions. Hence, we will focus more on the adsorbate configurations at low P_{CO} in the following calculations.

By inspecting the hydrogen distribution patterns for Ni and Ni_3Ga as displayed in the insets of Figures 2−4, a prominent difference in the ordering of surface *H species appears. The Ni surface is generally characteristic of irregular *H distribution, especially in that some of the *H atoms tend to be squeezed onto bridge sites. However, this does not occur on Ni_3Ga surface, and more importantly, the adsorbates at a coverage of 1/2 ML for *CH_x (x = 1−4) intermediates favor a highly symmetric and ordered distribution pattern that is similar to the configurations shown in Figure 1d,e. This ordering is even preserved during the C−C coupling process to reach *C_2 intermediates, as illustrated in Figure 5a−c. Here we consider the case of low P_{CO} and investigate the coupling of *C_1 species with another CO_2 after its first hydrogenation step, leading to a reaction intermediate of *C_1−COOH. Previous experiments suggested that the C−C coupling occurs with *COOH,[20,56−58] which is the main reason why we exemplify the modeling using this intermediate. Only *CHOH, *CH and *CH_2 are chosen as the initial *C_1 species because they are formed at a hydrogen coverage of around 1/2 ML. *CH_3 is not taken into consideration since we find that the pronounced steric hindrance of *CH_3 and *COOH will prevent their coupling. From the atomic environment of *CHOH−COOH, *CH−COOH and *CH_2−COOH, we can see that the highly ordered distribution of *H atoms are hardly affected by their interaction with the *C_2 intermediates, and this result holds in the process where *C_2 intermediates are further reduced into C_2 products (Figures S16 and S17).

In Figure 5d, we show that the kinetic barrier for the C−C coupling between *CHOH and *COOH is relatively high, consistent with the strong steric repulsion between both intermediates. However, when the steric effect is negligible between the *C_1 species, C−C coupling would become considerably more facile (e.g., between *CH and *COOH) or

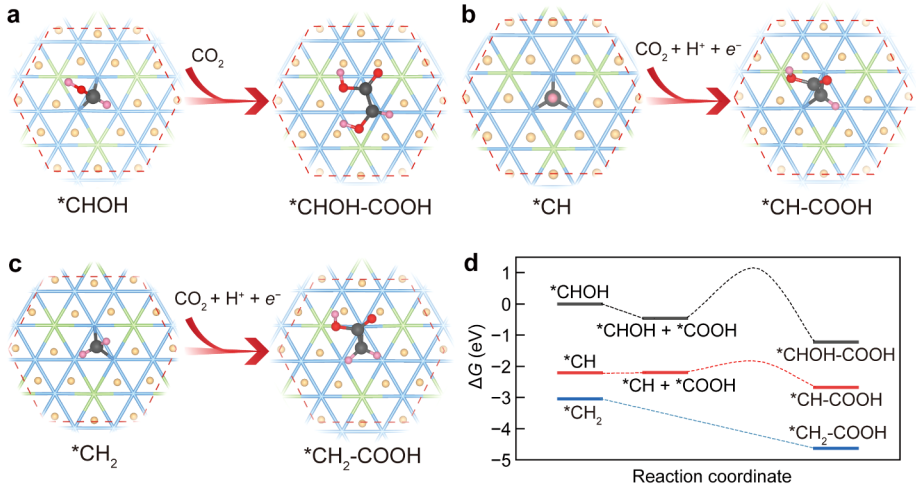

Figure 5. Incorporation of the second CO_2 to form *C_1−COOH on Ni_3Ga (111) surface with an adsorbate coverage of 1/2 ML at low P_{CO}. (a) *CHOH as the *C_1 participant. (b) *CH as the *C_1 participant. (c) *CH_2 as the *C_1 participant. (d) The kinetic energy barriers for the corresponding C−C coupling processes. The hydrogenation of the second CO_2 near *CHOH proceeds via the PT mechanism, leading to a change in the adsorbate coverage from 17/32 ML to 1/2 ML, while the hydrogenation step near *CH/*CH_2 proceeds via the PCET mechanism at 1/2 ML coverage. The configuration of *CH_2 + *COOH is unstable and will spontaneously transform into *CH_2−COOH.

https://doi.org/10.1021/acscatal.4c02126
ACS Catal. 2024, 14, 14330−14338

even barrierless (e.g., between *CH_2 and *COOH), which confers the ability to form C_{2+} products, as in line with the experimental results of Ni_3Ga catalyst.[12,18,19] Moreover, we have also calculated the kinetic barriers of *CH → *CH_2 and *CH_2 → *CH_3 steps, as shown in Figures S18 and S19. We find that the barrier of *CH hydrogenation (0.22 eV) is relatively lower than that for *CH + *COOH → *CH−COOH (0.41 eV). On the other hand, the barrier of *CH_2 hydrogenation is 0.36 eV, while the *CH_2 + *COOH → *CH_2−COOH step is spontaneous. Therefore, we may conclude that the *CH_2 species is more susceptible than other reaction intermediates to C−C coupling reaction when in competition with the hydrogenation step.

Dependence of C−C Coupling on Hydrogen Coverage. By combining the results of C−C coupling for both Ni (111) and Ni_3Ga (111) surfaces, we may elucidate the mechanism behind how hydrogen coverage on Ni-based catalysts steers the reaction pathways toward C_{2+} products. We first investigate the atomic structures of *C_1 + *COOH, in which the *COOH intermediate is formed by either PCET or PT mechanism via the reduction of the second CO_2 on the surface. DFT structural optimization of these configurations shows a major difference between both catalysts: on Ni surface, the distance between the two C atoms in *C_1 + *COOH is noticeably larger than that on Ni_3Ga (Figure 6a). This could be ascribed to the fact that the CO_2 reduction intermediates on Ni are always surrounded by *H in close vicinity, thus favoring a reaction path with each intermediate having only one metal−carbon bond so that more *H atoms could be accommodated at the hollow sites. As compared with the scenario of both *C_1 and *COOH located at neighboring top sites on Ni surface, the configurations of *C_1 at a hollow site near the *COOH at a top site on Ni_3Ga would definitely give rise to a much shorter C−C distance, which can reach as low as 70% of that on Ni at an adsorbate coverage of 1/2 ML.

A short C−C distance between the intermediates can raise the opportunity for efficient C−C coupling, while a longer distance would likely trigger the rearrangement of *H adsorbates during the movement of C atoms, which may disrupt the C−C coupling. The latter case is observed on Ni, where the *COOH adsorbate in *C_1 + *COOH configuration will easily transform into formic acid (HCOOH) when *COOH comes close to the nearby *C_1 intermediate (Figures 6b and S20). We note that this *COOH → HCOOH step proceeds via the PT mechanism, which is essentially associated with the strong propensity for *H to interact with the CO_2 reduction intermediates. In contrast, HCOOH formation is not directly observed on Ni_3Ga for the *C_1 + *COOH configurations examined in this work. Yet, by comparing the energetics between C−C coupling step and *COOH → HCOOH step for *C_1 + *COOH (Figure 6a), we find that the *C_1 intermediates formed at an adsorbate coverage of >1/2 ML tend to exhibit a substantial energetic driving force to turn the second CO_2 into HCOOH, thus rendering these *C_1 species incapable to form *C_2 in a selective manner (Figure 6c). When the adsorbate coverage is decreased to 1/2 ML, however, the *CH and *CH_2 intermediates unequivocally show that their coupling with *COOH is kinetically favorable (Figures 6d and S21) and the resultant *C_2 intermediates can be further reduced into C_2 products with a smooth downhill energy landscape (Figure S16).

We have also examined the kinetics of *H, *COOH and *CO on Ni (111) and Ni_3Ga (111) surfaces. Our results show

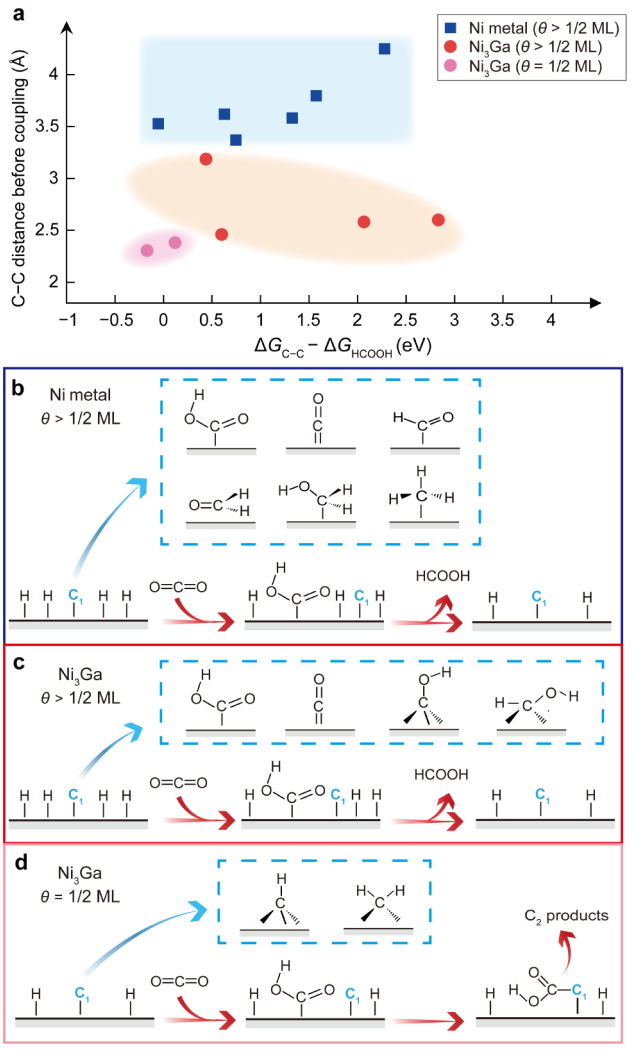

Figure 6. Mechanism of C−C coupling on Ni and Ni_3Ga. (a) The C−C distance for *C_1 + *COOH configurations, and the energy difference between C−C coupling (ΔG_{C-C}) and HCOOH formation (ΔG_{HCOOH}) on the (111) surfaces of Ni and Ni_3Ga at different adsorbate coverage (θ). (b-d) The reaction pathways of *C_1 + *COOH, in which *C_1 intermediates (shown in the blue dashed frame) are formed (b) on Ni at θ > 1/2 ML, (c) on Ni_3Ga at θ > 1/2 ML and (d) on Ni_3Ga at θ = 1/2 ML.

that on Ni, the kinetic barrier for *H migration from a Ni_3-hcp-hollow site to a nearby Ni_3-fcc-hollow site is only 0.19 eV (Figure S22), while on Ni_3Ga, the migration of *H from a Ni_2Ga-fcc-hollow site to a Ni_3-hcp-hollow site is barrierless. Therefore, the migration of *H adsorbates on both catalysts can be regarded as sufficiently facile to facilitate the PT process. On Ni, *COOH migrates between two neighboring Ni-top sites with a barrier of 0.13 eV (Figure S23), and *CO migrates from a Ni_3-hcp-hollow site to a nearby Ni_3-fcc-hollow site with a barrier of 0.16 eV (Figure S24). In contrast, *COOH migration on Ni_3Ga corresponds to a considerably high activation energy barrier of 0.59 eV (Figure S25), which will further increase to 1.03 eV for the migration from a Ni-top site to a Ga-top site (Figure S26). A similarly high barrier (0.60 eV) is also found for *CO migration from a Ni_3-hcp-hollow site to a Ni_2Ga-fcc-hollow site (Figure S27). The above results indicate that *COOH and *CO migration on Ni surface is much more facile than that on Ni_3Ga. However, the fast

https://doi.org/10.1021/acscatal.4c02126
ACS Catal. 2024, 14, 14330−14338

migration of $*C_1$ intermediates on Ni does not guarantee high opportunity for C−C coupling and C_2 production. From the thermodynamic calculation results displayed in Figure 6, we can see that despite their facile migration, the $*C_1$ species on Ni are not likely to move toward each other, and the large C−C distance will lead to a relatively low opportunity for coupling.

Overall, the above results indicate that the C−C coupling process depends significantly on the hydrogen coverage at which the corresponding $*C_1$ participants are finally formed. At a low coverage such as 1/2 ML, the distribution pattern of adsorbates is highly symmetric and well-ordered, which barely changes upon C−C coupling and in the subsequent reduction steps. This structure provides ample space above the Ni_3-hollow site for accommodating two $*C_1$ species with a short C−C distance during CO_2RR, which renders C−C coupling more competitive to take place than the formation of C_1 products. If such an ordered configuration no longer exists, as resulted from a high hydrogen coverage that typically occurs on Ni metal, then the direct translocation of *H to the $*C_1$ intermediates will overwhelm the C−C coupling process, thus hindering the formation of C_{2+} products. This could account for the low C_{2+} selectivity exhibited on Ni catalysts that have no extraneous elements. In this sense, Ga in Ni_3Ga can be regarded as a modulator of both surface hydrogen coverage and adsorbate distribution pattern on the exposed Ni atoms, which works in synergy with atom polarization effects and surface geometric factors to determine the efficiency of C−C coupling. We would also like to note that the modification of surface hydrogen on Ni-based catalysts is not restricted to the design of the catalyst itself, but can benefit from the electrolyte side. While increasing pH is not appropriate because it would hamper CO_2RR as well,[59] a proper selection of the salts and their concentration in the electrolyte may serve as a promising strategy for the tuning of proton supply to the metal surface, which is expected to share an intimate link to surface hydrogen coverage. Further investigation with combined theoretical and spectroscopic methods is required to better understand how the electric double layer controls the surface hydrogen distribution and the CO_2RR performance of Ni-based catalysts.

CONCLUSIONS

In summary, the current study reveals the indispensable role of surface hydrogen coverage and adsorbate distribution pattern in determining the reaction pathways of CO_2RR on Ni-based electrocatalysts. Taking Ni_3Ga as a model, we demonstrate that the incorporation of Ga atoms can afford a reduced *H coverage relative to the Ni metal catalyst, thus resulting in much weaker electrostatic interactions between the adsorbates. This enables an ordering of the *H species on Ni_3Ga under working conditions, which, however, does not occur on Ni. Owing to this difference, CO_2RR on Ni_3Ga adopts the C_{2+} pathway at the bifurcation between C−C coupling and excessive hydrogenation of the $*C_1$ intermediates, while Ni metal favors the latter and directs the reaction to C_1 products. Our DFT results not only support and rationalize the previous experimental finding of increased C_{2+} selectivity for Ni catalysts upon doping/alloying, but also provide a theoretical foundation for the strategy of adsorbate modification at catalyst-electrolyte interfaces to boost C−C coupling efficiency.

ASSOCIATED CONTENT

Supporting Information

The Supporting Information is available free of charge at https://pubs.acs.org/doi/10.1021/acscatal.4c02126.

Details of computational models and equations used for constructing Pourbaix diagrams, all adsorbate configurations for Pourbaix diagram calculations, complete free energy diagrams of CO_2RR and HER, the kinetic barriers of important reaction species, and adsorption configuration figures for CO_2RR (PDF)

AUTHOR INFORMATION

Corresponding Authors

Shisheng Zheng − *College of Energy, Xiamen University, Xiamen 361000, China*; Email: zhengss@pku.edu.cn

Shunning Li − *School of Advanced Materials, Peking University, Shenzhen Graduate School, Shenzhen 518055, China*; orcid.org/0000-0002-5381-6025; Email: lisn@pku.edu.cn

Feng Pan − *School of Advanced Materials, Peking University, Shenzhen Graduate School, Shenzhen 518055, China*; orcid.org/0000-0002-8216-1339; Email: panfeng@pkusz.edu.cn

Authors

Haowen Ding − *School of Advanced Materials, Peking University, Shenzhen Graduate School, Shenzhen 518055, China*

Xinzhe Yang − *School of Advanced Materials, Peking University, Shenzhen Graduate School, Shenzhen 518055, China*; orcid.org/0009-0008-1921-0629

Junjie Pan − *School of Advanced Materials, Peking University, Shenzhen Graduate School, Shenzhen 518055, China*

Zhefeng Chen − *School of Advanced Materials, Peking University, Shenzhen Graduate School, Shenzhen 518055, China*

Mingzheng Zhang − *School of Advanced Materials, Peking University, Shenzhen Graduate School, Shenzhen 518055, China*

Complete contact information is available at: https://pubs.acs.org/10.1021/acscatal.4c02126

Notes

The authors declare no competing financial interest.

ACKNOWLEDGMENTS

The authors acknowledge financial support from the Guangdong Basic and Applied Basic Research Foundation (2020A1515110843 and 2023A1515011391), the National Natural Science Foundation of China (22109003) and the Major Science and Technology Infrastructure Project of Material Genome Big-science Facilities Platform supported by Municipal Development and Reform Commission of Shenzhen.

REFERENCES

(1) Yan, T.; Chen, X.; Kumari, L.; Lin, J.; Li, M.; Fan, Q.; Chi, H.; Meyer, T. J.; Zhang, S.; Ma, X. Multiscale CO_2 Electrocatalysis to C_{2+} Products: Reaction Mechanisms, Catalyst Design, and Device Fabrication. *Chem. Rev.* **2023**, *123* (17), 10530−10583.

(2) Xie, Y.; Ou, P.; Wang, X.; Xu, Z.; Li, Y. C.; Wang, Z.; Huang, J. E.; Wicks, J.; McCallum, C.; Wang, N.; et al. High carbon utilization

in CO_2 reduction to multi-carbon products in acidic media. *Nat. Catal.* **2022**, *5* (6), 564−570.
(3) Wakerley, D.; Lamaison, S.; Wicks, J.; Clemens, A.; Feaster, J.; Corral, D.; Jaffer, S. A.; Sarkar, A.; Fontecave, M.; Duoss, E. B.; et al. Gas diffusion electrodes, reactor designs and key metrics of low-temperature CO_2 electrolysers. *Nat. Energy* **2022**, *7* (2), 130−143.
(4) Zhou, X.; Shan, J.; Chen, L.; Xia, B. Y.; Ling, T.; Duan, J.; Jiao, Y.; Zheng, Y.; Qiao, S.-Z. Stabilizing Cu_{2+} Ions by Solid Solutions to Promote CO_2 Electroreduction to Methane. *J. Am. Chem. Soc.* **2022**, *144* (5), 2079−2084.
(5) Wang, L.; Chen, W.; Zhang, D.; Du, Y.; Amal, R.; Qiao, S.; Wu, J.; Yin, Z. Surface strategies for catalytic CO_2 reduction: from two-dimensional materials to nanoclusters to single atoms. *Chem. Soc. Rev.* **2019**, *48* (21), 5310−5349.
(6) Zhu, Y.; Yang, X.; Peng, C.; Priest, C.; Mei, Y.; Wu, G. Carbon-Supported Single Metal Site Catalysts for Electrochemical CO_2 Reduction to CO and Beyond. *Small* **2021**, *17* (16), No. e2005148.
(7) Li, F.; Li, Y. C.; Wang, Z.; Li, J.; Nam, D.-H.; Lum, Y.; Luo, M.; Wang, X.; Ozden, A.; Hung, S.-F.; et al. Cooperative CO_2-to-ethanol conversion via enriched intermediates at molecule−metal catalyst interfaces. *Nat. Catal.* **2020**, *3* (1), 75−82.
(8) Zhang, T.; Bui, J. C.; Li, Z.; Bell, A. T.; Weber, A. Z.; Wu, J. Highly selective and productive reduction of carbon dioxide to multicarbon products via in situ CO management using segmented tandem electrodes. *Nat. Catal.* **2022**, *5* (3), 202−211.
(9) Zhuang, T.-T.; Pang, Y.; Liang, Z.-Q.; Wang, Z.; Li, Y.; Tan, C.-S.; Li, J.; Dinh, C. T.; De Luna, P.; Hsieh, P.-L.; et al. Copper nanocavities confine intermediates for efficient electrosynthesis of C_3 alcohol fuels from carbon monoxide. *Nat. Catal.* **2018**, *1* (12), 946−951.
(10) Das, S.; Perez-Ramirez, J.; Gong, J.; Dewangan, N.; Hidajat, K.; Gates, B. C.; Kawi, S. Core-shell structured catalysts for thermocatalytic, photocatalytic, and electrocatalytic conversion of CO_2. *Chem. Soc. Rev.* **2020**, *49* (10), 2937−3004.
(11) Jiang, Y.; Long, R.; Xiong, Y. Regulating C−C coupling in thermocatalytic and electrocatalytic CO_x conversion based on surface science. *Chem. Sci.* **2019**, *10* (31), 7310−7326.
(12) Paris, A. R.; Bocarsly, A. B. Mechanistic insights into C_2 and C_3 product generation using Ni_3Al and Ni_3Ga electrocatalysts for CO_2 reduction. *Faraday Discuss.* **2019**, *215*, 192−204.
(13) Calvinho, K. U. D.; Laursen, A. B.; Yap, K. M. K.; Goetjen, T. A.; Hwang, S.; Murali, N.; Mejia-Sosa, B.; Lubarski, A.; Teeluck, K. M.; Hall, E. S.; et al. Selective CO_2 reduction to C_3 and C_4 oxyhydrocarbons on nickel phosphides at overpotentials as low as 10 mV. *Energy Environ. Sci.* **2018**, *11* (9), 2550−2559.
(14) Paris, A. R.; Bocarsly, A. B. Ni−Al Films on Glassy Carbon Electrodes Generate an Array of Oxygenated Organics from CO_2. *ACS Catal.* **2017**, *7* (10), 6815−6820.
(15) Nitopi, S.; Bertheussen, E.; Scott, S. B.; Liu, X. Y.; Engstfeld, A. K.; Horch, S.; Seger, B.; Stephens, I. E. L.; Chan, K.; Hahn, C.; et al. Progress and Perspectives of Electrochemical CO_2 Reduction on Copper in Aqueous Electrolyte. *Chem. Rev.* **2019**, *119* (12), 7610−7672.
(16) Bagger, A.; Arnarson, L.; Hansen, M. H.; Spohr, E.; Rossmeisl, J. Electrochemical CO Reduction: A Property of the Electrochemical Interface. *J. Am. Chem. Soc.* **2019**, *141* (4), 1506−1514.
(17) Peterson, A. A.; Abild-Pedersen, F.; Studt, F.; Rossmeisl, J.; Nørskov, J. K. How copper catalyzes the electroreduction of carbon dioxide into hydrocarbon fuels. *Energy Environ. Sci.* **2010**, *3* (9), 1311−1315.
(18) Torelli, D. A.; Francis, S. A.; Crompton, J. C.; Javier, A.; Thompson, J. R.; Brunschwig, B. S.; Soriaga, M. P.; Lewis, N. S. Nickel−Gallium−Catalyzed Electrochemical Reduction of CO_2 to Highly Reduced Products at Low Overpotentials. *ACS Catal.* **2016**, *6* (3), 2100−2104.
(19) Paris, A. R.; Chu, A. T.; O'Brien, C. B.; Frick, J. J.; Francis, S. A.; Bocarsly, A. B. Tuning the Products of CO_2 Electroreduction on a Ni_3Ga Catalyst Using Carbon Solid Supports. *J. Electrochem. Soc.* **2018**, *165* (7), H385−H392.
(20) Zhou, Y.; Martín, A. J.; Dattila, F.; Xi, S.; López, N.; Pérez-Ramírez, J.; Yeo, B. S. Long-chain hydrocarbons by CO_2 electroreduction using polarized nickel catalysts. *Nat. Catal.* **2022**, *5* (6), 545−554.
(21) Saxena, A.; Liyanage, W. P. R.; Kapila, S.; Nath, M. Nickel selenide as an efficient electrocatalyst for selective reduction of carbon dioxide to carbon-rich products. *Catal. Sci. Technol.* **2022**, *12* (15), 4727−4739.
(22) Zhang, X.-D.; Liu, K.; Fu, J.-W.; Li, H.-M.; Pan, H.; Hu, J.-H.; Liu, M. Pseudo-copper Ni-Zn alloy catalysts for carbon dioxide reduction to C_2 products. *Front. Phys.* **2021**, *16* (6), 63500.
(23) Xiao, H.; Cheng, T.; Goddard, W. A.; Sundararaman, R. Mechanistic Explanation of the pH Dependence and Onset Potentials for Hydrocarbon Products from Electrochemical Reduction of CO on Cu (111). *J. Am. Chem. Soc.* **2016**, *138* (2), 483−486.
(24) Favaro, M.; Xiao, H.; Cheng, T.; Goddard, W. A., III; Yano, J.; Crumlin, E. J. Subsurface oxide plays a critical role in CO_2 activation by Cu(111) surfaces to form chemisorbed CO_2, the first step in reduction of CO_2. *Proc. Natl. Acad. Sci. U. S. A.* **2017**, *114* (26), 6706−6711.
(25) Cheng, T.; Xiao, H.; Goddard, W. A. Full atomistic reaction mechanism with kinetics for CO reduction on Cu(100) from ab initio molecular dynamics free-energy calculations at 298 K. *Proc. Natl. Acad. Sci. U. S. A.* **2017**, *114* (8), 1795−1800.
(26) Xiao, H.; Goddard, W. A.; Cheng, T.; Liu, Y. Cu metal embedded in oxidized matrix catalyst to promote CO_2 activation and CO dimerization for electrochemical reduction of CO_2. *Proc. Natl. Acad. Sci. U. S. A.* **2017**, *114* (26), 6685−6688.
(27) Zhou, Y.; Che, F.; Liu, M.; Zou, C.; Liang, Z.; De Luna, P.; Yuan, H.; Li, J.; Wang, Z.; Xie, H.; et al. Dopant-induced electron localization drives CO_2 reduction to C_2 hydrocarbons. *Nat. Chem.* **2018**, *10* (9), 974−980.
(28) Zhong, M.; Tran, K.; Min, Y.; Wang, C.; Wang, Z.; Dinh, C.-T.; De Luna, P.; Yu, Z.; Rasouli, A. S.; Brodersen, P.; et al. Accelerated discovery of CO_2 electrocatalysts using active machine learning. *Nature* **2020**, *581* (7807), 178−183.
(29) Zhuang, T.-T.; Liang, Z.-Q.; Seifitokaldani, A.; Li, Y.; De Luna, P.; Burdyny, T.; Che, F.; Meng, F.; Min, Y.; Quintero-Bermudez, R.; et al. Steering post-C−C coupling selectivity enables high efficiency electroreduction of carbon dioxide to multi-carbon alcohols. *Nat. Catal.* **2018**, *1* (6), 421−428.
(30) Zheng, S.; Liang, X.; Pan, J.; Hu, K.; Li, S.; Pan, F. Multi-Center Cooperativity Enables Facile C−C Coupling in Electrochemical CO_2 Reduction on a Ni_2P Catalyst. *ACS Catal.* **2023**, *13* (5), 2847−2856.
(31) Huang, L.; Li, D.; Tian, D.; Jiang, L.; Li, Z.; Wang, H.; Li, K. Optimization of Ni-Based Catalysts for Dry Reforming of Methane via Alloy Design: A Review. *Energy Fuels* **2022**, *36* (10), 5102−5151.
(32) Zhang, H.; Gao, J.; Raciti, D.; Hall, A. S. Promoting Cu-catalysed CO_2 electroreduction to multicarbon products by tuning the activity of H_2O. *Nat. Catal.* **2023**, *6* (9), 807−817.
(33) Gao, D.; Arán-Ais, R. M.; Jeon, H. S.; Roldan Cuenya, B. Rational catalyst and electrolyte design for CO_2 electroreduction towards multicarbon products. *Nat. Catal.* **2019**, *2* (3), 198−210.
(34) Deng, B.; Huang, M.; Zhao, X.; Mou, S.; Dong, F. Interfacial Electrolyte Effects on Electrocatalytic CO_2 Reduction. *ACS Catal.* **2022**, *12* (1), 331−362.
(35) Wang, Y. H.; Zheng, S.; Yang, W. M.; Zhou, R. Y.; He, Q. F.; Radjenovic, P.; Dong, J. C.; Li, S.; Zheng, J.; Yang, Z. L.; et al. In situ Raman spectroscopy reveals the structure and dissociation of interfacial water. *Nature* **2021**, *600* (7887), 81−85.
(36) Zang, Y.; Cai, J.; Han, Y.; Wu, H.; Zhu, W.; Shi, S.; Zhang, H.; Ran, Y.; Yang, F.; Ye, M.; et al. CO_2 Activation on Ni(111) and Ni(110) Surfaces in the Presence of Hydrogen. *J. Phys. Chem. Lett.* **2023**, *14* (19), 4381−4387.
(37) Feng, J.; Zhang, L.; Liu, S.; Xu, L.; Ma, X.; Tan, X.; Wu, L.; Qian, Q.; Wu, T.; Zhang, J.; et al. Modulating adsorbed hydrogen drives electrochemical CO_2-to-C_2 products. *Nat. Commun.* **2023**, *14* (1), 4615.

https://doi.org/10.1021/acscatal.4c02126
ACS Catal. 2024, 14, 14330−14338

(38) Banerjee, S.; Kakekhani, A.; Wexler, R. B.; Rappe, A. M. Mechanistic Insights into CO_2 Electroreduction on Ni_2P: Understanding Its Selectivity toward Multicarbon Products. *ACS Catal.* **2021**, *11* (18), 11706−11715.
(39) Greeley, J.; Mavrikakis, M. A first-principles study of surface and subsurface H on and in Ni(111): diffusional properties and coverage-dependent behavior. *Surf. Sci.* **2003**, *540* (2−3), 215−229.
(40) Ling, C.; Zhang, Y.; Li, Q.; Bai, X.; Shi, L.; Wang, J. New Mechanism for N_2 Reduction: The Essential Role of Surface Hydrogenation. *J. Am. Chem. Soc.* **2019**, *141* (45), 18264−18270.
(41) Ulissi, Z. W.; Tang, M. T.; Xiao, J.; Liu, X.; Torelli, D. A.; Karamad, M.; Cummins, K.; Hahn, C.; Lewis, N. S.; Jaramillo, T. F.; et al. Machine-Learning Methods Enable Exhaustive Searches for Active Bimetallic Facets and Reveal Active Site Motifs for CO_2 Reduction. *ACS Catal.* **2017**, *7* (10), 6600−6608.
(42) Hori, Y.; Kikuchi, K.; Suzuki, S. Production of CO and CH_4 in electrochemical reduction of CO_2 at metal electrodes in aqueous hydrogencarbonate solution. *Chem. Lett.* **1985**, *14* (11), 1695−1698.
(43) Hori, Y.; Murata, A. Electrochemical evidence of intermediate formation of adsorbed CO in cathodic reduction of CO_2 at a nickel electrode. *Electrochim. Acta* **1990**, *35* (11−12), 1777−1780.
(44) Vos, R. E.; Koper, M. T. M. Nickel as Electrocatalyst for $CO_{(2)}$ Reduction: Effect of Temperature, Potential, Partial Pressure, and Electrolyte Composition. *ACS Catal.* **2024**, *14*, 4432−4440.
(45) Granda-Marulanda, L. P.; Rendón-Calle, A.; Builes, S.; Illas, F.; Koper, M. T. M.; Calle-Vallejo, F. A Semiempirical Method to Detect and Correct DFT-Based Gas-Phase Errors and Its Application in Electrocatalysis. *ACS Catal.* **2020**, *10* (12), 6900−6907.
(46) Di Pierro, M.; Elber, R.; Leimkuhler, B. A Stochastic Algorithm for the Isobaric-Isothermal Ensemble with Ewald Summations for All Long Range Forces. *J. Chem. Theory Comput.* **2015**, *11* (12), 5624−5637.
(47) Hori, Y.; Wakebe, H.; Tsukamoto, T.; Koga, O. Electrocatalytic process of CO selectivity in electrochemical reduction of CO_2 at metal electrodes in aqueous media. *Electrochim. Acta* **1994**, *39* (11−12), 1833−1839.
(48) Koga, O; Hori, Y. Reduction of adsorbed CO on a Ni electrode in connection with the electrochemical reduction of CO_2. *Electrochim. Acta* **1993**, *38* (10), 1391−1394.
(49) Sandberg, R. B.; Montoya, J. H.; Chan, K.; Nørskov, J. K. CO-CO coupling on Cu facets: Coverage, strain and field effects. *Surf. Sci.* **2016**, *654*, 56−62.
(50) Preikschas, P.; Martín, A. J.; Yeo, B. S.; Pérez-Ramírez, J. NMR-based quantification of liquid products in CO_2 electroreduction on phosphate-derived nickel catalysts. *Commun. Chem.* **2023**, *6* (1), 147.
(51) Mitsui, T.; Rose, M. K.; Fomin, E.; Ogletree, D. F.; Salmeron, M. Hydrogen adsorption and diffusion on Pd(111). *Surf. Sci.* **2003**, *540* (1), 5−11.
(52) Thurmer, K.; Bartelt, N. C.; Whaley, J. A.; McDaniel, A. H.; El Gabaly, F. The role of H-H interactions and impurities on the structure and energetics of H/Pd(111). *J. Chem. Phys.* **2022**, *156* (4), 044707.
(53) Garza, A. J.; Bell, A. T.; Head-Gordon, M. Mechanism of CO_2 Reduction at Copper Surfaces: Pathways to C_2 Products. *ACS Catal.* **2018**, *8* (2), 1490−1499.
(54) Zhang, J.; Cai, W.; Hu, F. X.; Yang, H.; Liu, B. Recent advances in single atom catalysts for the electrochemical carbon dioxide reduction reaction. *Chem. Sci.* **2021**, *12* (20), 6800−6819.
(55) Choi, W.; Won, D. H.; Hwang, Y. J. Catalyst design strategies for stable electrochemical CO_2 reduction reaction. *J. Mater. Chem. A* **2020**, *8* (31), 15341−15357.
(56) Lin, W.-Y.; Chen, Z.-X.; Xiong, H.; Li, H.-C.; Ho, Y.-S.; Hsieh, C.-T.; Lu, Q.; Cheng, M.-J. Identification of CO_2 as a Reactive Reagent for C−C Bond Formation via Copper-Catalyzed Electrochemical Reduction. *ACS Catal.* **2023**, *13* (17), 11697−11710.
(57) Jiao, X.; Zheng, K.; Chen, Q.; Li, X.; Li, Y.; Shao, W.; Xu, J.; Zhu, J.; Pan, Y.; Sun, Y.; et al. Photocatalytic Conversion of Waste Plastics into C_2 Fuels under Simulated Natural Environment Conditions. *Angew. Chem., Int. Ed.* **2020**, *59* (36), 15497−15501.
(58) Wu, Y.; Chen, Q.; Zhu, J.; Zheng, K.; Wu, M.; Fan, M.; Yan, W.; Hu, J.; Zhu, J.; Pan, Y.; et al. Selective CO_2-to-C_2H_4 Photoconversion Enabled by Oxygen-Mediated Triatomic Sites in Partially Oxidized Bimetallic Sulfide. *Angew. Chem., Int. Ed.* **2023**, *62* (15), No. e202301075.
(59) Liu, X.; Schlexer, P.; Xiao, J.; Ji, Y.; Wang, L.; Sandberg, R. B.; Tang, M.; Brown, K. S.; Peng, H.; Ringe, S.; et al. pH effects on the electrochemical reduction of $CO_{(2)}$ towards C_2 products on stepped copper. *Nat. Commun.* **2019**, *10* (1), 32.

https://doi.org/10.1021/acscatal.4c02126
ACS Catal. 2024, 14, 14330−14338